Numerical solution of a highly nonlinear and non-integrable equation using integrated radial basis function network method

Rajeev P. Bhanot (iD), Dmitry V. Strunin (iD), and Duc Ngo-Cong (iD)

View Online   Export Citation   CrossMark

Numerical solution of a highly nonlinear and non-integrable equation using integrated radial basis function network method

Rajeev P. Bhanot,[1,2,a)] (ID) Dmitry V. Strunin,[2,b)] (ID) and Duc Ngo-Cong[3,4,c)] (ID)

AFFILIATIONS

[1] School of Chemical Engineering and Physical Sciences, Department of Mathematics, Lovely Professional University, Phagwara, Punjab 144411, India
[2] School of Sciences, Faculty of Health, Engineering and Sciences, University of Southern Queensland, Toowoomba, Queensland 4350, Australia
[3] Institute for Advanced Engineering and Space Sciences, University of Southern Queensland, Toowoomba, Queensland 4350, Australia
[4] School of Chemical Engineering, The University of Queensland, Brisbane, Queensland 4072, Australia

[a)] Author to whom correspondence should be addressed: rajeevbhanot@yahoo.com and rajeev.23674@lpu.co.in
[b)] Electronic mail: strunin@usq.edu.au
[c)] Electronic mail: ngocongduc@gmail.com

ABSTRACT

In this paper, we investigate a wide range of dynamical regimes produced by the nonlinearly excited phase (NEP) equation (a single sixth-order nonlinear partial differential equation) using a more advanced numerical method, namely, the integrated radial basis function network method. Previously, we obtained single-step spinning solutions of the equation using the Galerkin method. First, we verify the numerical solver through an exact solution of a forced version of the equation. Doing so, we compare the numerical results obtained for different space and time steps with the exact solution. Then, we apply the method to solve the NEP equation and reproduce the previously obtained spinning regimes. In the new series of numerical experiments, we find regimes in the form of spinning trains of steps/kinks comprising one, two, or three kinks. The evolution of the distance between the kinks is analyzed. Two different kinds of boundary conditions are considered: homogeneous and periodic. The dependence of the dynamics on the size of the domain is explored showing how larger domains accommodate multiple spinning fronts. We determine the critical domain size (bifurcation size) above which non-trivial settled regimes become possible. The initial condition determines the direction of motion of the kinks but not their sizes and velocities.

Published under license by AIP Publishing. https://doi.org/10.1063/5.0009215

Detonation waves, solid flames, and similar fronts of reaction in active-dissipative systems can be simulated by a single sixth-order nonlinear partial differential equation (PDE) also referred to as the nonlinearly excited phase (NEP) equation. The concerned equation was developed phenomenologically by Strunin to model the propagation of spinning waves on a hollow cylinder. It is very difficult to solve a highly nonlinear PDE especially when we lack its exact solution. To overcome this scenario, we took various initial conditions and demonstrate that regardless of different initial conditions, we are getting similar results. We will use our solver to solve complicated physical problems in future work.

I. INTRODUCTION

Formation of super-adiabatic structures in propagating reaction fronts, such as solid-phase combustion and spinning detonation, generated wide interest from theorists and applied mathematicians due to the rich spectrum of nonlinear effects. The original interest, however, was connected with practical applications including manufacturing of advanced materials by self-propagating high-temperature synthesis (SHS). For recent experimental research on the area, we refer to Refs. 1–3. Strunin in Ref. 4 designed a compact single-equation model capable of simulating the experimentally
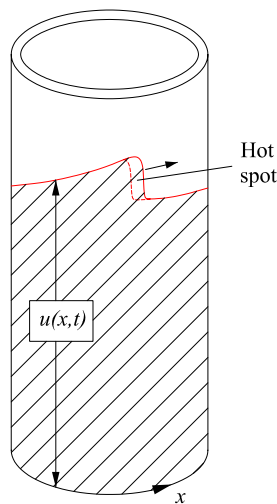
FIG. 1. A reaction front propagating on a hollow cylinder.

observed spinning reaction fronts on a cylinder,

$$\frac{\partial u}{\partial t} = -\left(\frac{\partial u}{\partial x}\right)^2 \frac{\partial^2 u}{\partial x^2} + \left(\frac{\partial u}{\partial x}\right)^4 + \frac{\partial^6 u}{\partial x^6}. \qquad (1.1)$$

Later on,[5] Eq. (1.1) was also shown to describe nonlinear instabilities in some non-local reaction–diffusion systems. In connection with those systems and for brevity, we will refer to Eq. (1.1) as the nonlinearly excited phase (NEP) equation.

In the context of the combustion fronts of the present paper, u stands for the distance passed by the front (approximately a line separating cold unburned mixture from hot burned products) along the axis of a hollow cylinder (Fig. 1).

The model (1.1) gives rise to rich dynamics of which the spinning front is one of the most spectacular regimes observed experimentally. Figure 1 sketches the kink shaped solution (1.1). The steep, almost vertical sections in (1.1) correspond, in experiments, to luminous hot spots. The spots have a very high temperature often called in combustion literature super-adiabatic. Similar hot-spot structures have also been found in experiments with infiltration combustion.[3]

Special attention was drawn recently to the structures of combustion fronts in heterogeneous reactive compositions. Regardless of the effect of initial perturbations, the combustion process can be accompanied by the spontaneous formation of regular structures, the symmetry of which differs from the symmetry of initial conditions. For systems in which the reactive gas is blown through the reaction products in the direction of the propagating front, it was shown in Ref. 6 that the combustion process may become unstable, accompanied by the formation of finger-shaped structures. These processes were experimentally studied in Ref. 7 for the propagation of a smoldering wave in a slit-like channel filled with sawdust. The focus was on examining the effect of scale factors on the loss of stability of the combustion of highly porous media. The structuring of the combustion front in metal powders subject to natural gas infiltration was theoretically and experimentally investigated

in Refs. 1–3. The authors analyzed the infiltration combustion of porous media and the dynamics of initiation and propagation of cellular wave structures. They studied the dependence of the number and shape of cells on the governing thermo-physical parameters of the heterogeneous medium, the geometric characteristics of the porous composition, heat loss, etc. These studies showed that the planar front may break into individual cells, which move through the condensed material layer in the pulsation mode, leaving behind a band of condensed combustion products with a periodic structure.

Qualitative character of these regimes can be simulated using Eq. (1.1). The equation is based on phenomenological principles: it mimics the evolution of the shape of the front[4] while leaving the concentration and temperature as such outside the scope of consideration. In support of a phenomenological approach, we note that combustion systems are often extremely complex and may involve chains of chemical reactions between numerous reactants complicated by mechanical deformations, melting, etc. This may render prohibitively difficult to model the combustion systems using the basic heat and concentration equations. As an example of using a phenological approach, we refer to Refs. 8 and 9 where the long-term cluster evolution in granular gases was studied.

For the spinning waves of combustion, the first attempt to construct a model based on phenomenological principles was made by Aldushin et al.[10] However, the model (1.1) better describes the shape of the front.[4] In Ref. 10, the shape is sinusoidal, whereas in Ref. 4, it is kink-like just as observed experimentally. In addition, the motion of the kink decays completely if affected by a sufficiently strong heat loss into the outside medium, also in agreement with the experiments. In terms of the derivative, $v = \partial u/\partial x$, the kink has the form of a soliton. To be precise, it is an auto-soliton—a type of solitons encountered in active physical and biological systems.[11,12] The prefix auto- distinguishes this type of solitons from the solitons in conservative systems. While the conservative solitons result from the balance between nonlinearity and dispersion, the auto-solitons result from the balance between energy release and dissipation. The combustion front is a typical example of an active-dissipative system, where the energy is produced by chemical reactions and the dissipation is facilitated by thermoconductivity. An auto-soliton possesses a unique amplitude and unique velocity as dictated by the energy balance. In Eq. (1.1), the energy release is represented by the term $(\partial u/\partial x)^2 \partial^2 u/\partial x^2$ and the dissipation represented by the term $\partial^6 u/\partial x^6$. The term $(\partial u/\partial x)^4$ links the release and dissipation.[4,5,13]

For the convenience of computations, we rewrite Eq. (1.1) as

$$\frac{\partial u}{\partial t} = -A\left(\frac{\partial u}{\partial x}\right)^2 \frac{\partial^2 u}{\partial x^2} + B\left(\frac{\partial u}{\partial x}\right)^4 + C\frac{\partial^6 u}{\partial x^6}, \qquad (1.2)$$

where A and C are positive and B is assumed positive for convenience (the case of $B < 0$ is converted to the case of $B > 0$ by transforming $u \rightarrow -u$ and $B \rightarrow -B$).

By choosing different values of A, B, and C, we will achieve reasonably short duration of our experiments and good accuracy. However, we note that Eq. (1.2) can be transformed to the canonical form (1.1) by re-scaling u, x, and t. Therefore, the results of each of our experiments will also represent the solutions of the canonical equation (1.1) in re-scaled coordinates.

Previously, Eq. (1.1) was solved using the spectral Galerkin method[4] and the finite difference scheme,[13] and a few initial results were discussed in Ref. 14 using the 1D-IRBFN method. In the present paper, we use a more accurate method, which is a collocation method based on integrated radial basis function networks,[15,16] called the IRBFN method. As detailed in the Appendix, the method is particularly effective for solving equations with high-order derivatives. In Sec. II, we discretize Eq. (1.2). The method was previously verified in different applied areas of mechanics and physics; however, in Sec. III, we present our own verification by applying the method to a forced NEP equation with the exact solution. Then, in Sec. V, we use the method to obtain an analysis of a range of dynamics generated by the NEP equation (1.2), using different initial and boundary conditions. Conclusions are given in Sec. VI.

II. DISCRETIZATION OF THE GOVERNING EQUATION FOR SPINNING REACTION FRONTS

In this section, we discretize the governing equation (1.2) for spinning reaction fronts using the integrated radial basis function network (IRBFN) method[15,16] in conjunction with the Crank–Nicolson method. The spatial derivatives of the function $u(x)$, including the first- to sixth-order derivatives, are discretized using the IRBFN method as shown in the Appendix. Applying the Crank–Nicolson method[17] for the temporal discretization of Eq. (1.2) results in

$$
\frac{u^{(n+1)} - u^{(n)}}{\Delta t} = \frac{1}{2} \left[-A \left(\frac{\partial u}{\partial x} \right)^2 \frac{\partial^2 u}{\partial x^2} + B \left(\frac{\partial u}{\partial x} \right)^4 + C \frac{\partial^6 u}{\partial x^6} \right]^{(n)}
$$
$$
+ \frac{1}{2} \left[-A \left(\frac{\partial u}{\partial x} \right)^2 \frac{\partial^2 u}{\partial x^2} + B \left(\frac{\partial u}{\partial x} \right)^4 + C \frac{\partial^6 u}{\partial x^6} \right]^{(n+1)},
$$
(2.1)

where $\Delta t = t^{(n+1)} - t^{(n)}$ is the time step and the superscripts (n) and $(n + 1)$ denote the previous and current time levels, respectively. To linearize the nonlinear terms on the right hand side (RHS) of Eq. (2.1), we use a one-step Picard iteration method,[17,18]

$$
\frac{u^{(n+1)} - u^{(n)}}{\Delta t} = \frac{1}{2} \left[-A \left(\frac{\partial u}{\partial x} \right)^2 \frac{\partial^2 u}{\partial x^2} + B \left(\frac{\partial u}{\partial x} \right)^4 + C \frac{\partial^6 u}{\partial x^6} \right]^{(n)}
$$
$$
+ \frac{1}{2} \left[-A \left(\frac{\partial u^{(n)}}{\partial x} \right)^2 \frac{\partial^2 u^{(n+1)}}{\partial x^2} \right.
$$
$$
\left. + B \left(\frac{\partial u^{(n)}}{\partial x} \right)^3 \frac{\partial u^{(n+1)}}{\partial x} + C \frac{\partial^6 u^{(n+1)}}{\partial x^6} \right].
$$
(2.2)

Making use of Eqs. (A12)–(A16) to determine the spatial derivatives on the RHS of Eq. (2.2), we obtain

$$
\left\{ \frac{\mathbf{H}_0}{\Delta t} - \frac{1}{2} \left[-A \left(\mathbf{H}_1 \widehat{w}^{(n)} \right)^2 \mathbf{H}_2 + B \left(\mathbf{H}_1 \widehat{w}^{(n)} \right)^3 \mathbf{H}_1 + C \mathbf{H}_6 \right] \right\} \widehat{w}^{(n+1)}
$$
$$
= \left\{ \frac{\mathbf{H}_0}{\Delta t} + \frac{1}{2} \left[-A \left(\mathbf{H}_1 \widehat{w}^{(n)} \right)^2 \mathbf{H}_2 + B \left(\mathbf{H}_1 \widehat{w}^{(n)} \right)^3 \mathbf{H}_1 + C \mathbf{H}_6 \right] \right\} \widehat{w}^{(n)}.
$$
(2.3)

For simplicity, the above equation can be rewritten as

$$
\mathbf{E}_1 \widehat{w}^{(n+1)} = RHS_1.
$$
(2.4)

In the present study, we consider different sets of boundary conditions, namely,

- Set 1:

$$
u(x = L_1) = a_0, \; u(x = L_2) = b_0,
$$
(2.5)

$$
\frac{\partial u}{\partial x}(x = L_1) = a_1, \; \frac{\partial u}{\partial x}(x = L_2) = b_1,
$$
(2.6)

$$
\frac{\partial^2 u}{\partial x^2}(x = L_1) = a_2, \; \frac{\partial^2 u}{\partial x^2}(x = L_2) = b_2.
$$
(2.7)

- Set 2:

$$
\frac{\partial u}{\partial x}(x = L_1) = a_1, \; \frac{\partial u}{\partial x}(x = L_2) = b_1,
$$
(2.8)

$$
\frac{\partial^2 u}{\partial x^2}(x = L_1) = a_2, \; \frac{\partial^2 u}{\partial x^2}(x = L_2) = b_2,
$$
(2.9)

$$
\frac{\partial^3 u}{\partial x^3}(x = L_1) = a_3, \; \frac{\partial^3 u}{\partial x^3}(x = L_2) = b_3.
$$
(2.10)

- Set 3: Periodic boundary condition

$$
u(x = L_1) = u(x = L_2), \; \frac{\partial u}{\partial x}(x = L_1) = \frac{\partial u}{\partial x}(x = L_2),
$$
(2.11)

$$
\frac{\partial^2 u}{\partial x^2}(x = L_1) = \frac{\partial^2 u}{\partial x^2}(x = L_2), \; \frac{\partial^3 u}{\partial x^3}(x = L_1) = \frac{\partial^3 u}{\partial x^3}(x = L_2),
$$
(2.12)

$$
\frac{\partial^4 u}{\partial x^4}(x = L_1) = \frac{\partial^4 u}{\partial x^4}(x = L_2), \; \frac{\partial^5 u}{\partial x^5}(x = L_1) = \frac{\partial^5 u}{\partial x^5}(x = L_2),
$$
(2.13)

where $a_0, a_1, a_2, a_3, b_0, b_1, b_2,$ and b_3 are set numbers. The boundary conditions can be described by

$$
\mathbf{E}_2 \widehat{w}^{(n+1)} = RHS_2.
$$
(2.14)

The system of equations (2.4) and (2.14) is solved simultaneously at each time step for $\widehat{w}^{(n+1)}$ until the prescribed time $T_{\max}$ is reached. We then obtain all the values $u^{(n+1)}$ by substituting $\widehat{w}^{(n+1)}$ in Eq. (A11).

III. VERIFICATION OF THE IRBFN METHOD USING THE FORCED NEP EQUATION

In this section, we demonstrate the accuracy of our IRBFN solver using a forced NEP equation. The forced NEP equation is constructed with the purpose of allowing an exact solution, which, if

stable, should be captured by the numerical method. Therefore, we consider the equation

$$\frac{\partial u}{\partial t} = -A\left(\frac{\partial u}{\partial x}\right)^2 \frac{\partial^2 u}{\partial x^2} + B\left(\frac{\partial u}{\partial x}\right)^4 + C\frac{\partial^6 u}{\partial x^6} + f(x,t) \qquad (3.1)$$

and require that it has the exact solution

$$u = \sin(x - t). \qquad (3.2)$$

By substituting (3.2) into (3.1), we find the force,

$$f(x,t) = -\cos(x-t) - A\sin(x-t)\cos^2(x-t)$$
$$- B\cos^4(x-t) + C\sin(x-t). \qquad (3.3)$$

Choosing $A = 2$, $B = 1$, and $C = 1$, we consider Set 1 (2.5)–(2.7) and Set 2 (2.8)–(2.10) as the boundary conditions with the parameters a_0, a_1, a_2, a_3, b_0, b_1, b_2, and b_3 calculated using the exact solution (3.2). We evaluate the performance of the IRBFN solver based on the relative error norm, Ne, and the convergence rate $O(h^\alpha)$,

$$\mathrm{Ne} = \sqrt{\frac{\sum_{i=1}^{N}(u_i - \overline{u}_i)^2}{\sum_{i=1}^{N}\overline{u}_i^2}}, \qquad (3.4)$$

$$\mathrm{Ne}(h) \approx \gamma h^\alpha = O(h^\alpha), \qquad (3.5)$$

where u_i and $\overline{u}_i$ are the numerical and exact solutions at the ith node, respectively; h the grid size; and γ and α are exponential model's parameters.

Figure 2 gives the comparison between the exact solution and the IRBFN result at the time moment $t = 5.0$ for the two sets of boundary conditions, using a grid of 100 and $\Delta t = 0.001$. It appears that the IRBFN results are in good agreement with the exact solution. The relative error norm Ne(u) is 1.31×10^{-4} and 2.26×10^{-2}

FIG. 3. Experiments with the forced NEP equation: Grid convergence study of the solution u. The convergence rate is $O(h^{1.51})$ for Set 1 and $O(h^{1.99})$ for Set 2.

for Set 1 and Set 2, respectively. Figure 3 presents the grid convergence study of the numerical solution u. The convergence rate is $O(h^{1.51})$ for Set 1 and $O(h^{1.99})$ for Set 2.

Figure 4 shows the influence of the time step Δt on the solution accuracy Ne(u) for different grid sizes and sets of boundary conditions. We observe that the solution accuracy improves with reducing time step Δt until a certain value Δt_{opt}. The value Δt_{opt} reduces with increasing N. For Set 1, $\Delta t_{opt} = \{5 \times 10^{-3}, 2 \times 10^{-3}, 1 \times 10^{-3}, 5 \times 10^{-4}\}$ for $N = \{200, 400, 600, 800\}$, respectively. For Set 2, $\Delta t_{opt} = \{5 \times 10^{-3}, 2 \times 10^{-3}, 1 \times 10^{-3}, 2 \times 10^{-4}\}$ for $N = \{200, 400, 600, 800\}$, respectively.

IV. RESOLVING DISSIPATIVE STRUCTURE AND BIFURCATION LENGTH

In this section, we present results of a series of numerical experiments with different initial and boundary conditions and various lengths of spatial domain, L, as described in Table I.

A. Formation of a moving front

In Experiment 1, the equation coefficients are chosen as $A = 2$, $B = 1$, and $C = 1$. We use Set 2 boundary conditions, (2.8)–(2.10), with $a_1 = 0$, $a_2 = 0$, $a_3 = 0$, $b_1 = 0$, $b_2 = 0$, and $b_3 = 0$, $L = L_2 - L_1 = 15\pi$, $N = 100$ grid points, and time step $\Delta t = 0.001$. We use this time step in all our numerical experiments below. After some transitional period of evolution [Fig. 5(a)], the front clearly settles in a constant shape (most evident at the later moments), with the nearly horizontal tails as is seen from Fig. 5(b). See the ripples ahead of the main front [Fig. 5(b)]. This is typical when dissipation is expressed by a high-order derivative, in our case $\partial^6 u/\partial x^6$. Effectively, this regime represents an isolated step of Fig. 1. In Sec. IV B, we present further comparison between our results and the periodic solution from Fig. 1.
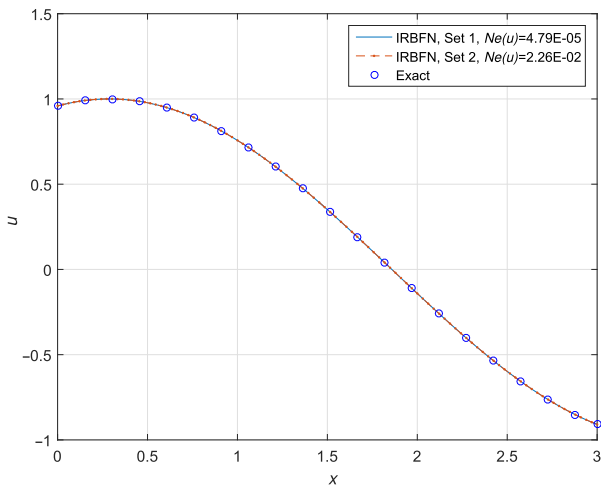

FIG. 2. Experiments with the forced NEP equation: Comparison between the exact solution and the IRBFN solution at $t = 5.0$ for two sets of boundary conditions using a grid of 100 and $\Delta t = 10^{-3}$.
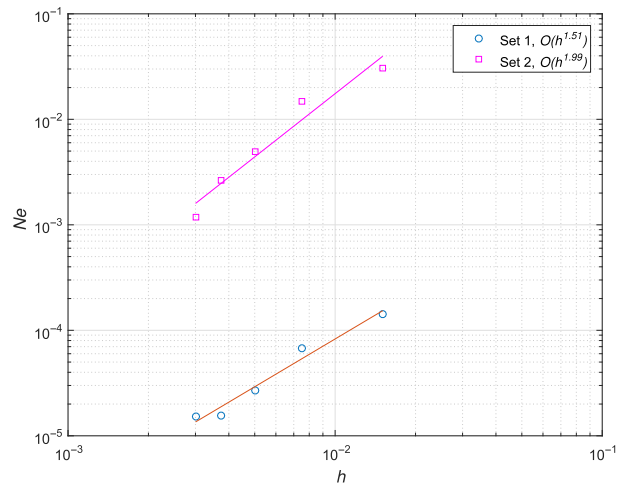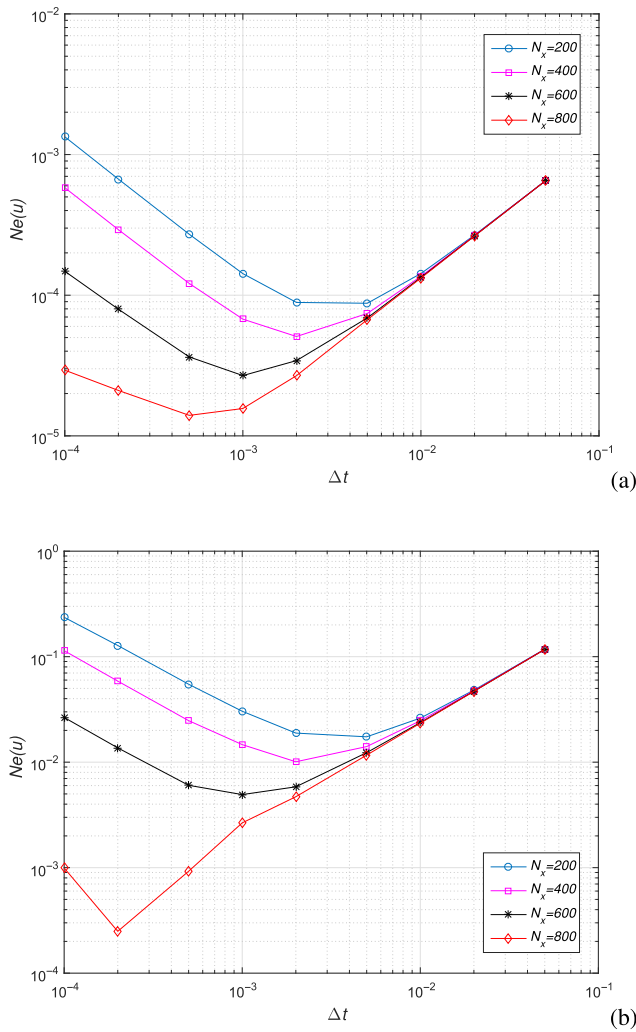
FIG. 4. Experiments with the forced NEP equation: Variation of $Ne(u)$ against Δt for different grid sizes for the boundary condition (a) Set 1 and (b) Set 2.

TABLE I. Resolving dissipative structures and bifurcation length: initial conditions, boundary conditions, and the length of computational domain L for different experiments. l stands for the bifurcation length.

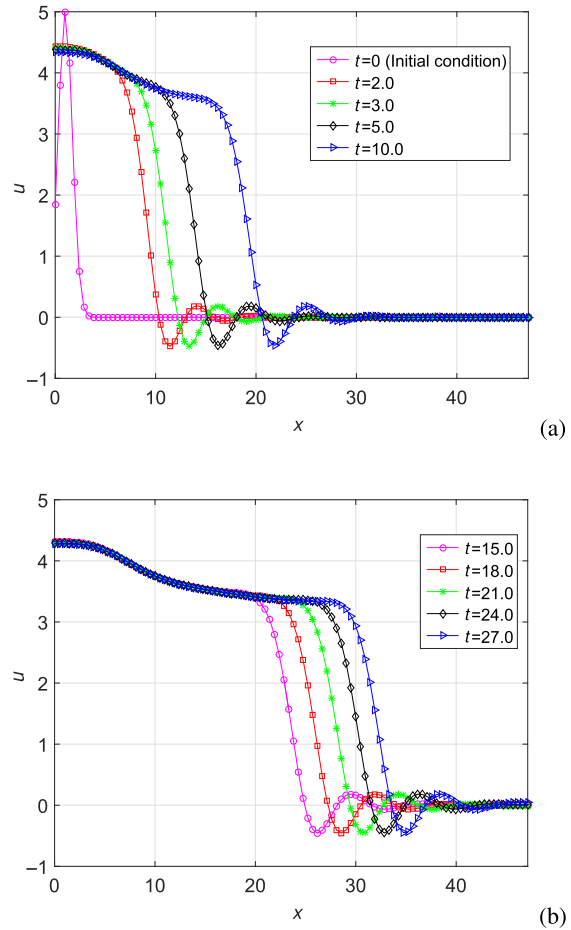| Experiment	Initial condition $u(x, 0)$	Boundary condition	Domain length L
1: A moving front	$5\exp\left[-(x-1)^2\right]$	Set 2	15π
2: A decaying wave	$\sin x$	Set 3	π
3: A decaying wave	$10\sin x$	Set 3	π
4: Bifurcation length	$1.1\left[\sin(3x)+\right.$ $\left.+\frac{1}{2}\sin(4x)+\frac{x}{8}\right]$	Set 3	$16.1 <$ $l < 16.2$

FIG. 5. Experiment 1: (a) The solution u vs x at different time moments during the transitional stage and (b) the settled stage.

B. Determination of bifurcation length

For the NEP equation, a dissipative structure is formed when all the three terms on the right-hand side of the equation balance each other. Denoting the characteristic amplitude of the structure by $U > 0$ and its characteristic length by $\ell > 0$, we have

$$\left(\frac{\partial u}{\partial x}\right)^2 \frac{\partial^2 u}{\partial x^2} \sim \frac{U^3}{l^4}, \left(\frac{\partial u}{\partial x}\right)^4 \sim \frac{U^4}{l^4}, \frac{\partial^6 u}{\partial x^6} \sim \frac{U}{l^6}. \quad (4.1)$$

The balance between the terms gives the two equations,

$$AU^3/\ell^4 \sim BU^4/\ell^4 \sim CU/\ell^6,$$

which determine the scales of the dissipative structure. When the length L is smaller than the length ℓ, there is not enough room for the structure to form. In this case, the dissipation term dominates over the energy release, and the system is driven toward decay. Figures 6 and 7 demonstrate such a decay. In Experiment 2, the equation coefficients are $A = 1$, $B = 1$, and $C = 1$. In this numerical experiment,
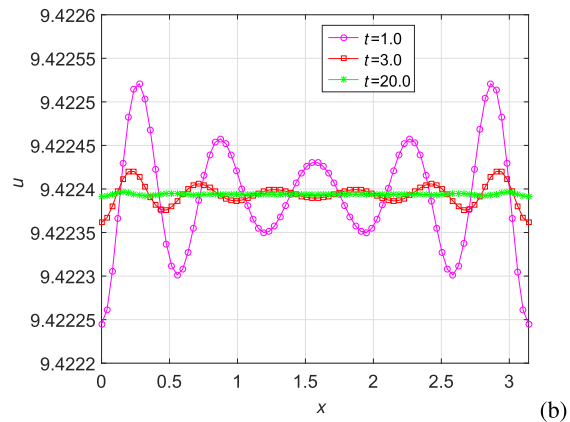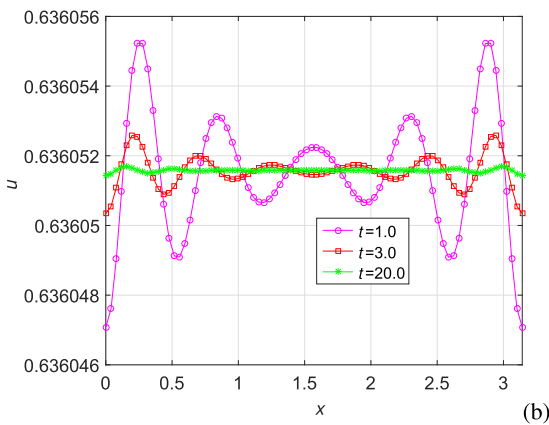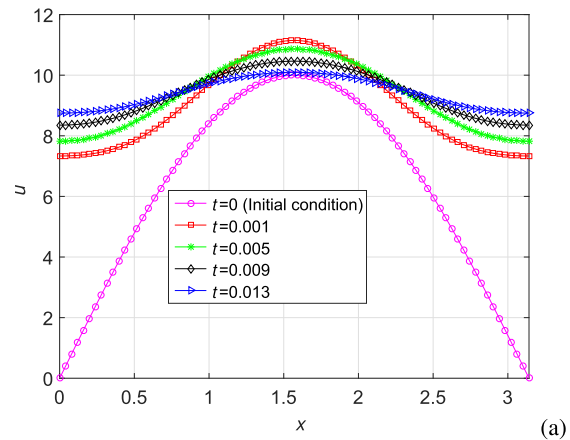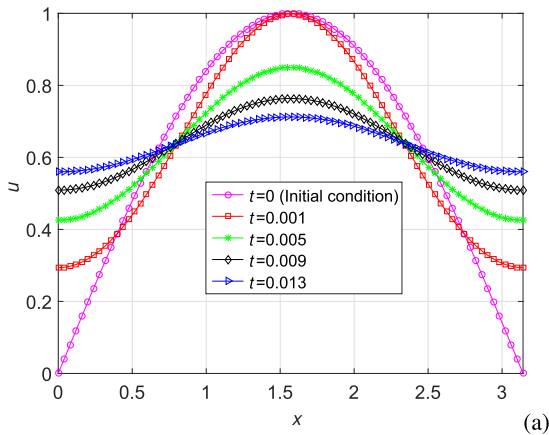
FIG. 6. Experiment 2: (a) The solution u vs x at different time moments during the transitional stage and (b) the decaying stage.

FIG. 7. Experiment 3: (a) The solution u vs x at different time moments during the transitional stage and (b) the decaying stage.

the solution is periodic in space; therefore, the boundary conditions are represented by Set 3, (2.11)–(2.13).

In Experiment 3 conducted with the same length $L = \pi$, we use the initial condition of a larger amplitude, namely, $u_0 = 10 \sin x$, compared to $u_0 = \sin x$ of Experiment 2. Despite the larger initial amplitude, the dynamic still decays; see Figs. 7(a) and 7(b).

Our main goal in this section is to determine the critical domain size $L = \ell$ (bifurcation length) such that for $L > \ell$, a nontrivial settled regime may form, and for $L < \ell$, only a trivial (spatially flat) settled state is possible. As before, we use periodic boundary conditions, Set 3.

To determine the critical transition from the decaying wave to the spinning wave regime, we conducted Experiment 4 using the domain length L varying from 15 to 17 with a spatial step $\Delta L = 0.5$. We found that the bifurcation length L is in the range from 16.0 to 16.5. To be more accurate, we used a finer step $\Delta L = 0.1$ for L varying from 16.0 to 16.5 and found that the L value is in the range from 16.1 to 16.2 as shown in Table II. In Experiment 4 with $A = 6$, $B = 2$, $C = 2$, and $L = 15$, the step-like structure does not appear

(Fig. 8) despite we run the experiment for a long period of time ($T_{\max} = 200$).

In Fig. 9, we present the behavior of u for $L = 16$, $L = 16.1$, and $L = 16.2$. In these experiments to keep the uniformity, we use $A = 6$,

TABLE II. Experiment 4: Determination of the bifurcation length.

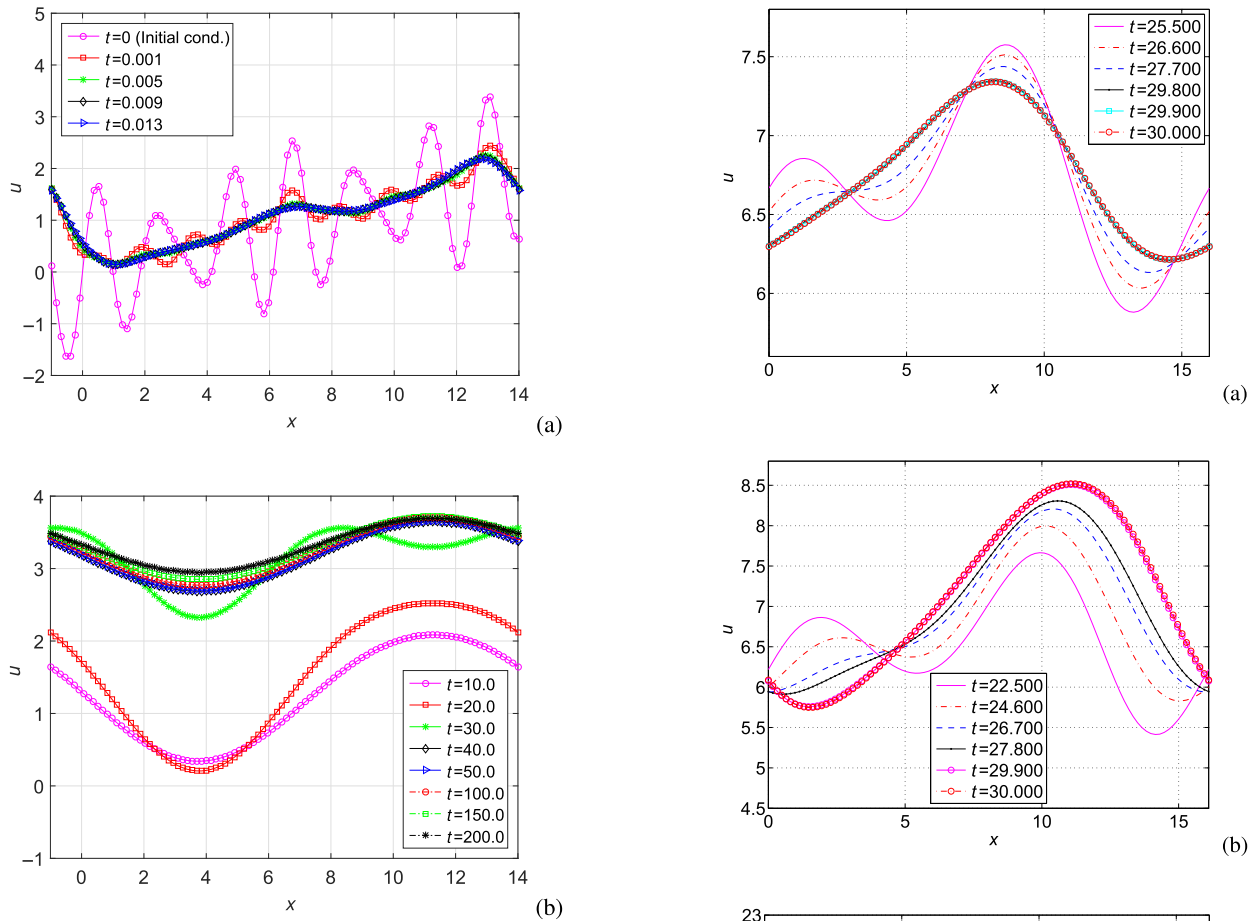| Domain length L	Solution regime
15	Decaying
15.5	Decaying
16	Decaying
16.1	Decaying
16.2	Spinning wave
16.3	Spinning wave
16.4	Spinning wave
16.5	Spinning wave
17	Spinning wave

FIG. 8. Experiment 4 with $L = 15$: (a) The solution u vs x at different time moments during the transitional stage and (b) the decaying stage.

$B = 2$, and $C = 2$ and take the same initial condition. The boundary conditions are represented by Set 3, the time step is $\Delta t = 0.001$, and the experiments were run until $T_{\max} = 30$. From Figs. 9(a) and 9(b) ($L = 16$ and $L = 16.1$, respectively), we see that the humps start to disappear and merge to a single hump. The formed hump slowly moves in a vertical direction and then decays as time passes. From Fig. 9(c) ($L = 16.2$), we observe that around $t = 20$, the initial humps created by the initial condition disappear and merge to a single hump, which then moves on a helical path as a spinning wave.

In order to obtain a sustaining structure, we increased the domain length to $L = 17$. Figures 10(a) and 10(b) show the corresponding behavior of $u(x, t)$. After some transitional period [Fig. 10(a)], a single step-like structure eventually settles as shown in Fig. 10(b). The wave survives and finally develops into a strong spinning wave moving to the right and up as time goes. This is the spinning regime similar to the one shown in Fig. 1. Thus, from this series of experiments, we determined that the bifurcation length lies in the interval $16.1 < \ell < 16.2$.
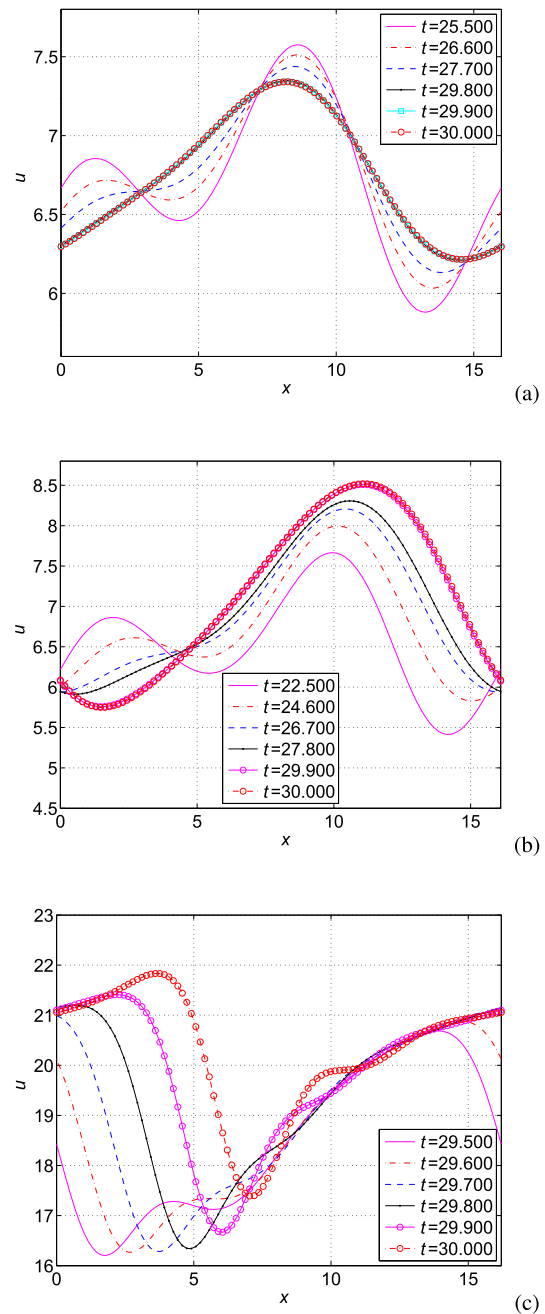

FIG. 9. Experiment with $L = 16$, $L = 16.1$, and $L = 16.2$: (a) The solution u vs x for $L = 16$, (b) the solution u vs x for $L = 16.1$, and (c) the solution u vs x for $L = 16.2$.

We note that the values of the equation coefficients A, B, and C are generally different in different experiments. In each experiment, they are selected as is convenient to achieve fast convergence of the dynamic to a settled state.
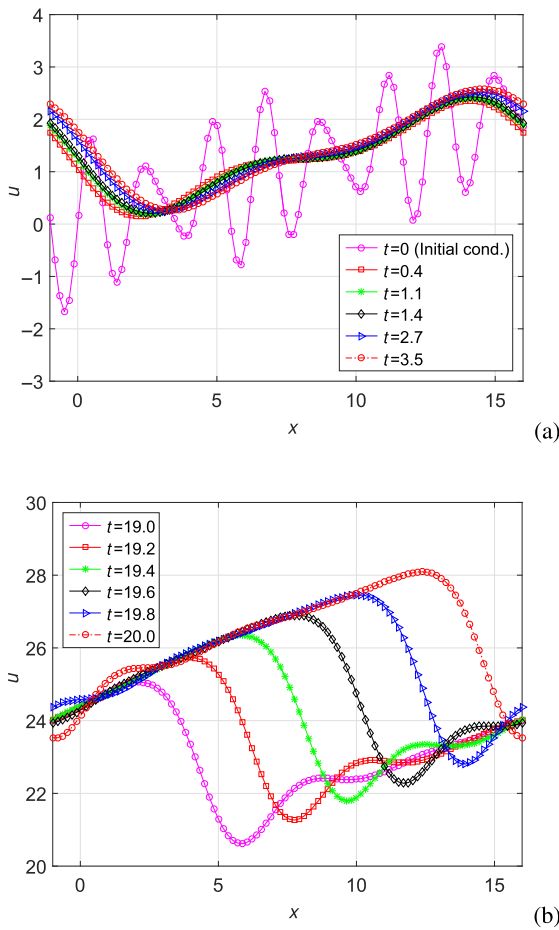
FIG. 10. Experiment 4 with $L = 17$: (a) The solution u vs x at different time moments during the transitional stage and (b) the settled stage.

We prefer, however, to translate the above result to one pertinent to a canonical form of Eq. (1.2), that is, Eq. (1.1). The canonical form is obtained by scaling u, x, and t to eliminate the coefficients A, B, and C as follows. Defining the scaled variables,

$$u = aU, \quad x = bX, \quad t = cT, \qquad (4.2)$$

we transform Eq. (1.2) to

$$\frac{\partial U}{\partial T} = -A \frac{a^2 c}{b^4} \left(\frac{\partial U}{\partial X} \right)^2 \frac{\partial^2 U}{\partial X^2} + B \frac{a^3 c}{b^4} \left(\frac{\partial U}{\partial X} \right)^4 + C \frac{c}{b^6} \frac{\partial^6 U}{\partial X^6}. \quad (4.3)$$

We make each coefficient equal to 1,

$$\frac{A a^2 c}{b^4} = 1, \quad \frac{B a^3 c}{b^4} = 1, \quad \frac{C c}{b^6} = 1, \qquad (4.4)$$

by choosing

$$a = \frac{A}{B}, \quad b = B \left(\frac{C}{A^3} \right)^{1/2}, \quad c = \frac{C^2 B^6}{A^7}. \qquad (4.5)$$

Using (4.2), the canonical length, l_{can}, is

$$l_{can} = l/b. \qquad (4.6)$$

Substituting $l = 16.1$ and $l = 16.2$ as well as $A = 6$, $B = 2$, and $C = 2$ into (4.5) and (4.6), we get $l_{can} = 83.65$ for $l = 16.1$ and $l_{can} = 84.177$ for $l = 16.2$. Hence, the bifurcation length lies within the interval $83.65 < l_{can} < 84.177$.

V. SPINNING WAVE REGIMES

For experiments in this section, in order to obtain spinning regimes, we choose the length of the spatial domain larger than the bifurcation length; i.e., the domain canonical length is chosen larger than the bifurcation canonical length ($83.65 < l_{can} < 84.177$) as shown in Table III. Table III presents the initial conditions, boundary conditions, the domain length L, b value, and the associated length L_{can} for different experiments. We emphasize again that concrete values of the equation coefficients A, B, and C are not important in terms of the shape of the front and the way it moves because each of the presented graphs of $u(x,t)$ can be treated as one corresponding to the canonical form of Eq. (1.2), only in scaled coordinates.

A. Single-step regime

In this subsection, we conduct three numerical experiments under periodic boundary conditions (Set 3) and with different initial conditions as described in Table III. The experiments produce a solution in the form of a single-step spinning front.

1. Experiment 1

The equation coefficients are $A = 8$, $B = 3$, and $C = 2$. The initial condition, $u(x,0) = 2 \sin x$, is periodic and, hence, is consistent with the boundary conditions. The dynamics survives apparently because L is larger than the bifurcation length. After some transitional period [Fig. 11(a)], the wave dynamic becomes settled as shown in Fig. 11(b); this is a single-step structure. In spite of the symmetry of the initial condition, the wave ends up moving to the left, not to the right. It appears that an ideally symmetric regime is intrinsically unstable; hence, it eventually evolves into one of the two possible asymmetric regimes (left-directed in this case).

2. Experiment 2

We use the parameters $A = 6$, $B = 2$, and $C = 2$. The initial condition is

$$u(x,0) = 1.1 \left[\sin(3x) + \frac{1}{2} \sin(4x) + \frac{x}{8} \right]. \qquad (5.1)$$

In this particular experiment, the initial condition does not satisfy the boundary conditions because at $t = 0$, the values of the function on the left end and on the right end of the domain are not the same. However, immediately after the start of the experiment, the solution $u(x,t)$ is forced to satisfy the boundary condition, creating the large step on the left. The dissipation quickly smoothens out the initial short-wavelength unevenness [Fig. 12(a)]. After a while, the settled spinning regime, a one-step structure, establishes with the direction of motion to the right [Fig. 12(c)].

TABLE III. Spinning wave regimes: initial conditions, boundary conditions, and the domain length L, b value, and the associated length L_{can} for different experiments.

Experiment	Initial condition $u(x, 0)$	Boundary condition	Domain length L	b	Domain canonical length $L_{can} = L/b$
1: Single-step regime	$2\sin x$	Set 3	25	0.188	133.333
2: Single-step regime	$1.1\left[\sin(3x) + \frac{1}{2}\sin(4x) + \frac{x}{8}\right]$	Set 3	12π	0.192	195.890
3: Single-step regime	$6.1\frac{\exp[0.25(x+1.1)] - \exp[-0.25(x+1.1)]}{\exp[0.25(x+1.1)] + \exp[-0.5(x+1.1)]}$	Set 3	9π	0.177	159.944
4: Two-step regime	$7.8\exp\left[-(x-5)^2\right]$	Set 2	70	0.354	197.990
5: Two-step regime	$2\sin x$	Set 3	55	0.188	293.333
6: Three-step regime	$8.2\exp\left[-(x-4)^2\right]$	Set 2	90	0.354	254.558

3. Experiment 3

The equation coefficients are chosen as $A = 4$, $B = 1$, and $C = 2$. Figure 13(a) shows the contour plot of $u(x, t)$ using a grid of 100. Figure 13(b) shows the dynamics at early times, while Fig. 13(c) shows the solution during the settled state. The front survives and moves up and to the right as time goes. The regime obtained here can
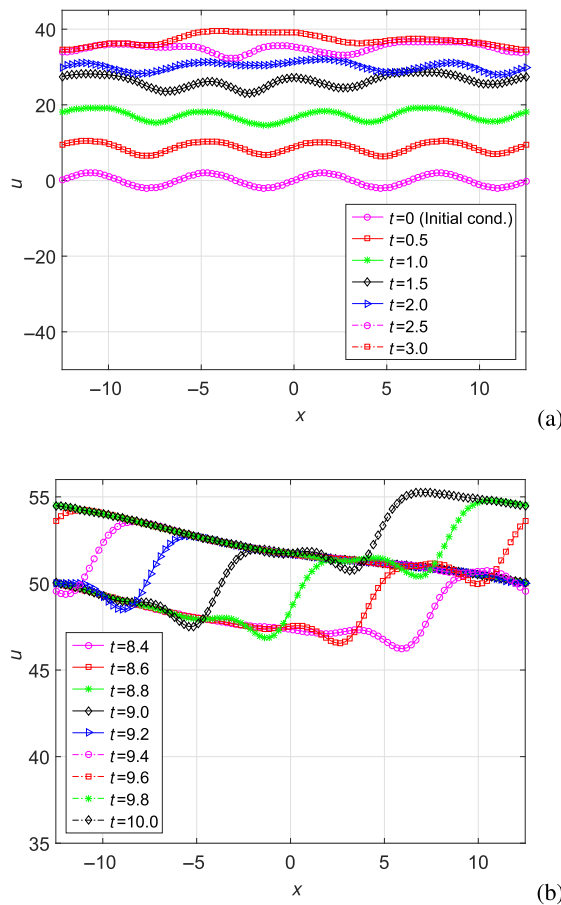
be associated with the reaction front moving in the spinning fashion on a cylindrical surface, where the x-coordinate is directed along the perimeter of the cylinder.

In this experiment, again, the initial condition is not consistent with the periodic boundary conditions. However, the solution $u(x, t)$ is immediately forced to satisfy boundary conditions, creating the large step on the left. This step is opposite in orientation (u decreases against x) to the step in the middle of the computational domain as part of the initial condition (u increases against x). As a result, an intensive energy release starts to act within the region of the large newly formed step, pushing the front to the right. This motion happens to be powerful enough for the new step to climb over the initial step in the middle and continue to move on top of it. Eventually, the right-moving spinning regime settles; see Fig. 13(c).

B. Two-step regime

In this section, we use larger computational domain in experiments with homogeneous (Set 2) and periodic (Set 3) boundary conditions.

1. Experiment 4: Homogeneous boundary conditions

The equation coefficients are chosen as $A = 2$, $B = 1$, and $C = 1$. Figure 14(a) presents the contour plot of $u(x, t)$. The initial condition is chosen in the form of a tall peak positioned near the left end of the domain. Because of the proximity of the left boundary, the peak can only move to the right. As the amplitude of the initial peak is sufficiently large, it transforms into not one, but two kinks. The lower kink leads the configuration, and the higher kink follows on top of it. After some transitional period [Fig. 14(b)], the two-kink structure settles as shown in Fig. 14(c).

2. Experiment 5: Periodic boundary conditions

The equation coefficients are chosen as $A = 8$, $B = 3$, and $C = 2$. Figure 15(a) presents the contour plot of $u(x, t)$. The initial condition has a sinusoidal form with several oscillations per period. The spatial domain is larger than that in the one-step regime (Experiment 1). After some transitional dynamics [Fig. 15(b)], the structures take a mature form around $t = 21$. A joined formation of two kinks moves from left to upper right, which represents a helical path when the figure plane is rolled into a cylinder [Fig. 15(c)].
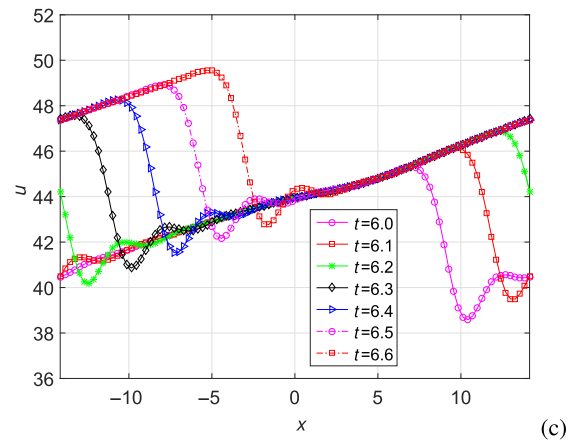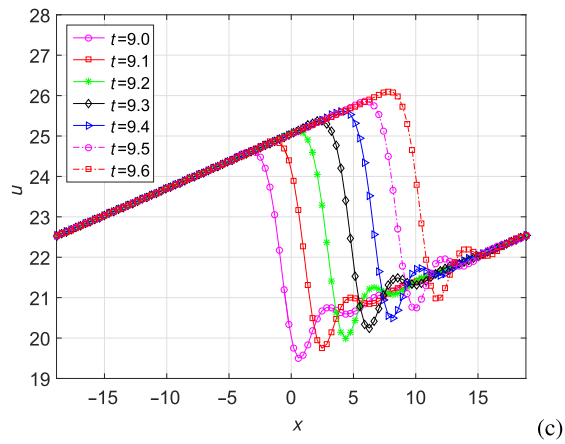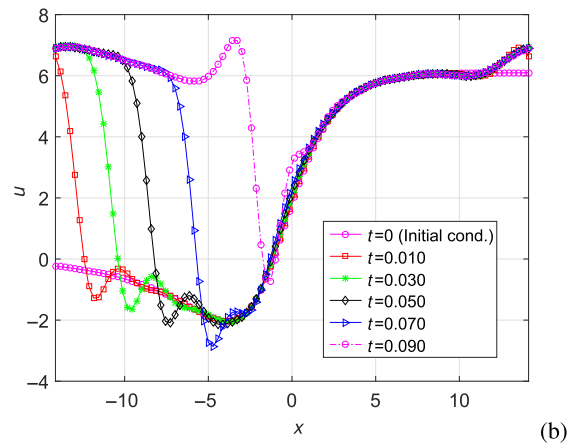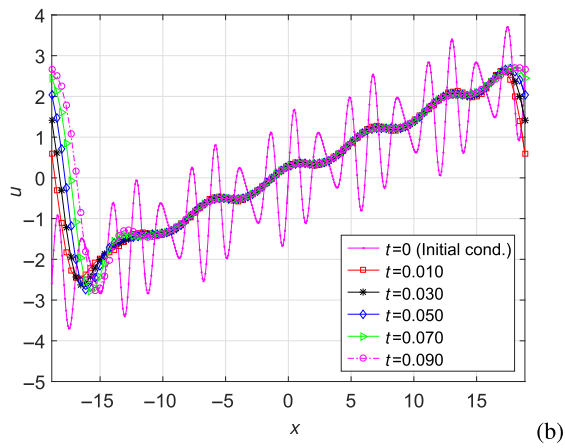

FIG. 11. Experiment 1: (a) The solution u vs x at different time moments during the transitional stage and (b) the settled stage.
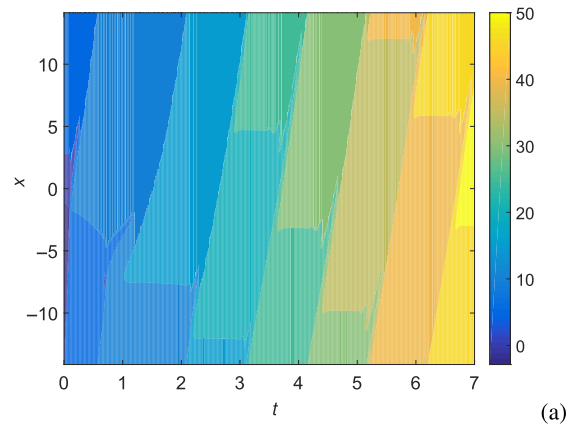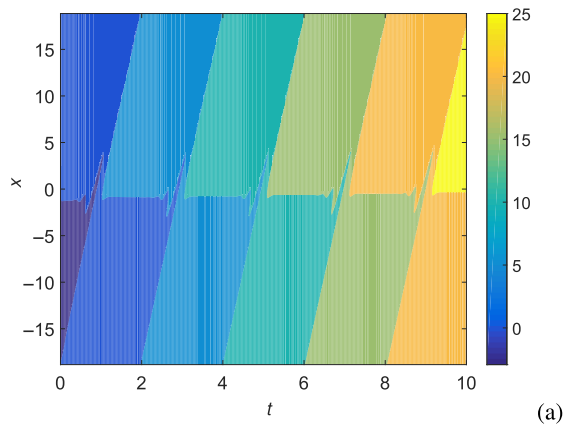
FIG. 12. Experiment 2: (a) Contour plot of $u(x, t)$, (b) the solution u vs x at different time moments during the transitional stage, and (c) the settled stage.

FIG. 13. Experiment 3: (a) Contour plot of $u(x, t)$, (b) the solution u vs x at different time moments during the transitional stage, and (c) the settled stage.
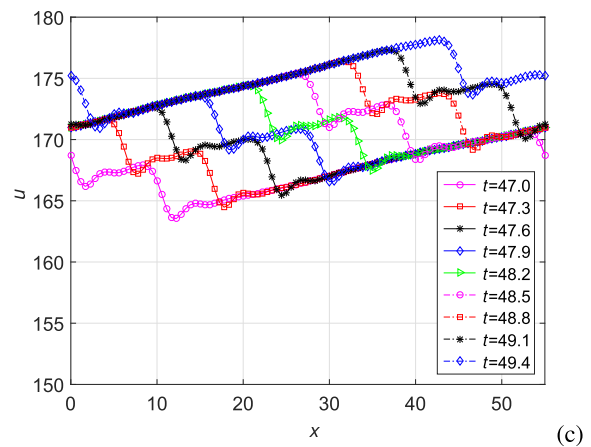
FIG. 14. Experiment 4: (a) Contour plot of $u(x, t)$, (b) the solution u vs x at different time moments during the transitional stage, and (c) the settled stage.

FIG. 15. Experiment 5: (a) Contour plot of $u(x, t)$, (b) the solution u vs x at different time moments during the transitional stage, and (c) the settled stage.
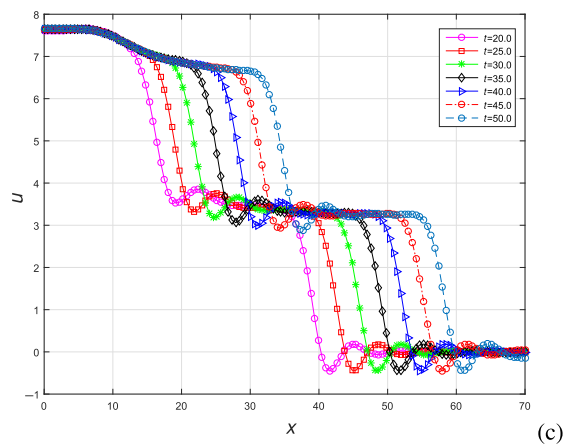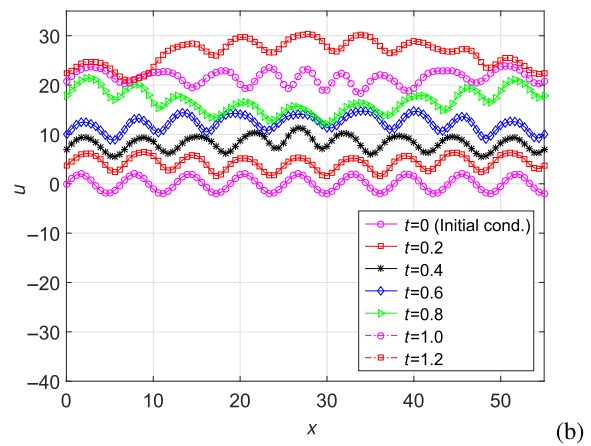
FIG. 16. Experiment 6: (a) Contour plot of $u(x, t)$, (b) the solution u vs x at different time moments during the transitional stage, and (c) the settled stage.
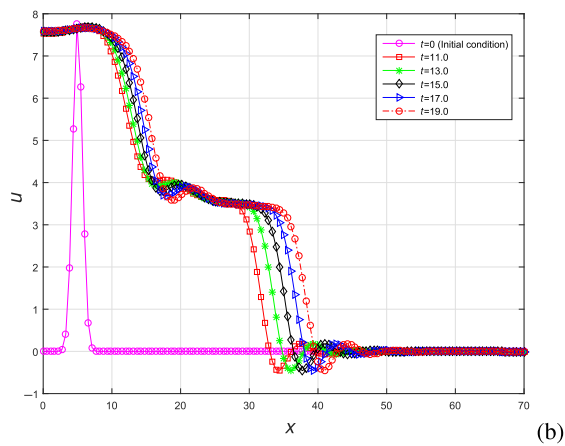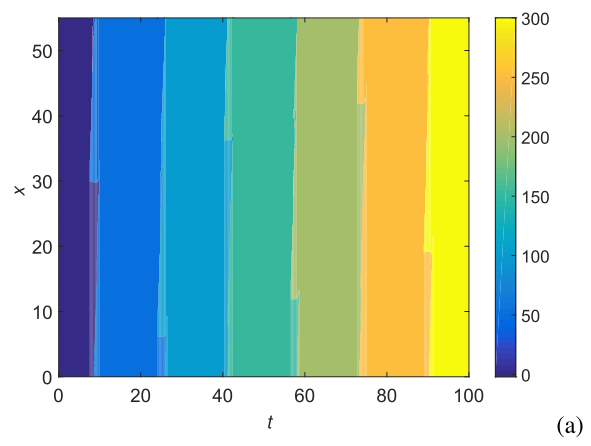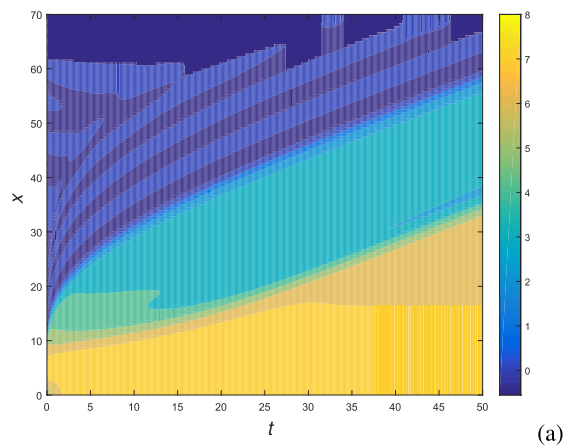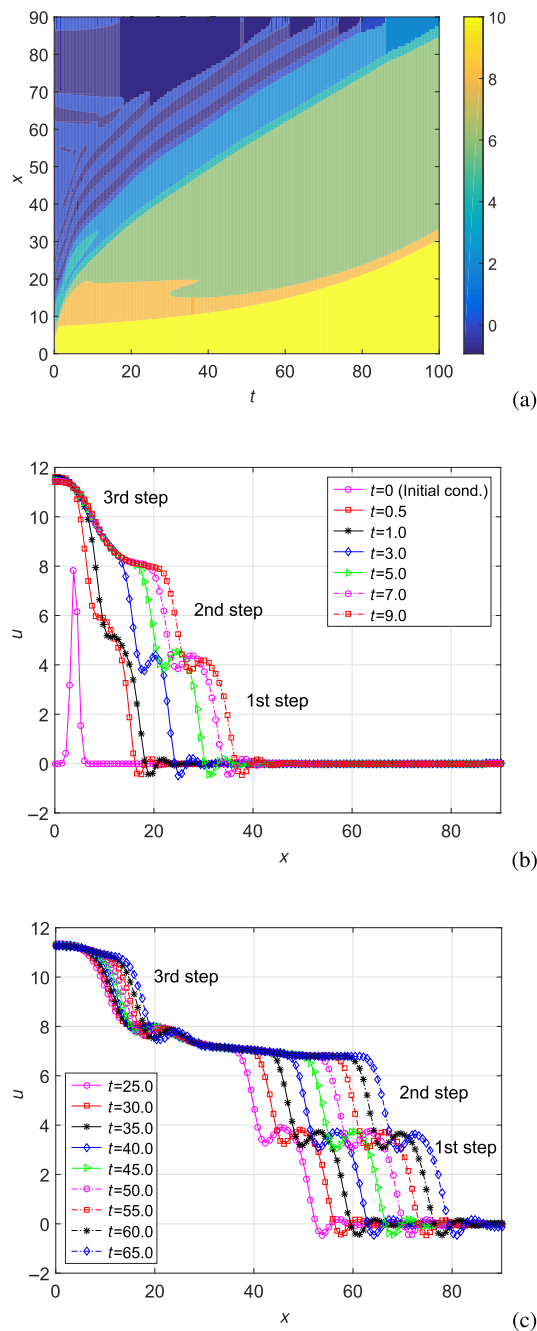
C. Three-step regime with homogeneous boundary conditions

In Experiment 6, the amplitude of the initial condition and the domain size are larger than those used in all the previous experiments. The equation coefficients are $A = 2$, $B = 1$, and $C = 1$. Relative to Experiment 4, the initial amplitude is increased from 7.8 to 8.2. This helps, alongside the larger domain available, to create the third step as shown in Figs. 16(a) and 16(b). After some transitional period [Fig. 16(b)], the three-step structure gradually appears as illustrated by Fig. 16(c). Observe the two fully formed leading steps with distinct horizontal plateaus, while the third step is in its formation stage. Notice that the highest point of the first step sits right on the crest of the small sub-peak in front of the second step. It would be interesting to investigate whether such a tight formation (between the first and second steps) is the closest possible; we leave this question for further study.

VI. CONCLUSIONS

We applied the IRBFN method in conjunction with the one-step Picard iteration method to solve the NEP equation simulating a combustion front propagation. The method successfully reproduced the spinning regimes, previously obtained in Ref. 4 using the Galerkin numerical method. A far wider variety of the dynamics are studied in the present paper. We used two types of boundary conditions—homogeneous and periodic—and different initial conditions. The single-step regimes are obtained in Experiments 1, 2, and 3, two-step regimes in Experiments 4 and 5, and three-step regimes in Experiment 6. We observed the complex process of formation of the spinning motion where the balance between the nonlinear energy release and high-order linear dissipation controls the dynamics. The direction of the spinning motion is controlled either by the asymmetry of the initial condition, or in the case of the symmetric initial condition, by instability of the symmetric regime. We determined the bifurcation length of the spatial domain, beyond which nontrivial settled dynamics are possible and below which only a trivial (no-motion) settled regime may form.

APPENDIX: THE IRBFN METHOD FOR SPATIAL DISCRETIZATION

Here, we briefly describe the IRBFN method,[15,16] which is used for spatial discretization of the NEP equation in the present study. The 1D domain ($L_1 < x < L_2$) is discretized by using a uniform grid with N nodes. Following the basic idea of the integral RBF method,[15] we decompose the highest pth-order derivative ($p = 6$ in our case) of the function u into RBFs,

$$\frac{\partial^p u}{\partial x^p} = \sum_{i=1}^{N} w_i G_i(x) = \sum_{i=1}^{N} w_i I_i^{(p)}(x), \tag{A1}$$

where $[w_i]_{i=1}^N$ is the set of network weights to be determined and $[G_i(x)]_{i=1}^N = [I_i^{(p)}(x)]_{i=1}^N$ is the set of known RBFs. Among possible RBFs, the multiquadric (MQ) functions are ranked as the most accurate and possess an exponential convergence with the spatial discretization refinement.[19] Therefore, we select the MQ functions for the computations. The MQ functions are given by $G_i(x) = \sqrt{(x - c_i)^T(x - c_i) + a_i^2}$, where c_i is called the center and a_i the RBF width determined as the distance between the ith center and its nearest neighbor.

Based on Eq. (A1), the lower-order derivatives and the function itself are then obtained through integration as follows:

$$\frac{\partial^{p-1} u}{\partial x^{p-1}} = \sum_{i=1}^N w_i I_i^{(p-1)}(x) + c_1, \tag{A2}$$

$$\frac{\partial^{p-2} u}{\partial x^{p-2}} = \sum_{i=1}^N w_i I_i^{(p-2)}(x) + c_1 x + c_2, \tag{A3}$$

$$\cdots\cdots\cdots$$

$$\frac{\partial^3 u}{\partial x^3} = \sum_{i=1}^N w_i I_i^{(3)}(x) + c_1 \frac{x^{p-4}}{(p-4)!} + c_2 \frac{x^{p-5}}{(p-5)!}$$
$$+ \cdots + c_{p-4} x + c_{p-3}, \tag{A4}$$

$$\frac{\partial^2 u}{\partial x^2} = \sum_{i=1}^N w_i I_i^{(2)}(x) + c_1 \frac{x^{p-3}}{(p-3)!} + c_2 \frac{x^{p-4}}{(p-4)!}$$
$$+ \cdots + c_{p-3} x + c_{p-2}, \tag{A5}$$

$$\frac{\partial u}{\partial x} = \sum_{i=1}^N w_i I_i^{(1)}(x) + c_1 \frac{x^{p-2}}{(p-2)!} + c_2 \frac{x^{p-3}}{(p-3)!}$$
$$+ \cdots + c_{p-2} x + c_{p-1}, \tag{A6}$$

$$u = \sum_{i=1}^N w_i I_i^{(0)}(x) + c_1 \frac{x^{p-1}}{(p-1)!} + c_2 \frac{x^{p-2}}{(p-2)!} + \cdots + c_{p-1} x + c_p, \tag{A7}$$

where $I_i^{(p-1)}(x) = \int I_i^{(p)}(x)dx$, $I_i^{(p-2)}(x) = \int I_i^{(p-1)}(x)dx, \ldots, I_i^{(0)}(x) = \int I_i^{(1)}(x)dx$ and $c_1, c_2, \ldots, c_p$ are the constants of integration.

The evaluation of (A1)–(A7) at a set of collocation points $[x_j]_{j=1}^N$ leads to

$$\widehat{\frac{\partial^p u}{\partial x^p}} = \widehat{\mathbf{I}^{(p)}} \widehat{w}, \tag{A8}$$

$$\widehat{\frac{\partial^{p-1} u}{\partial x^{p-1}}} = \widehat{\mathbf{I}^{(p-1)}} \widehat{w}, \tag{A9}$$

$$\cdots\cdots\cdots$$

$$\widehat{\frac{\partial u}{\partial x}} = \widehat{\mathbf{I}^{(1)}} \widehat{w}, \tag{A10}$$

$$\widehat{u} = \widehat{\mathbf{I}^{(0)}} \widehat{w}, \tag{A11}$$

where $\widehat{w} = (w_1, w_2, \ldots, w_{N_x}, c_1, c_2, \ldots, c_p)^T$, and

$$\widehat{\mathbf{I}^{(p)}} = \begin{bmatrix} I_1^{(p)}(x_1) & I_2^{(p)}(x_1) & \ldots & I_N^{(p)}(x_1) & 0 & 0 & \ldots & 0 & 0 \\ I_1^{(p)}(x_2) & I_2^{(p)}(x_2) & \ldots & I_N^{(p)}(x_2) & 0 & 0 & \ldots & 0 & 0 \\ \cdots\cdots\cdots\cdots\cdots\cdots\cdots\cdots\cdots\cdots \\ I_1^{(p)}(x_N) & I_2^{(p)}(x_N) & \ldots & I_N^{(p)}(x_N) & 0 & 0 & \ldots & 0 & 0 \end{bmatrix},$$

$$\widehat{\mathbf{I}^{(p-1)}} = \begin{bmatrix} I_1^{(p-1)}(x_1) & I_2^{(p-1)}(x_1) & \ldots & I_N^{(p-1)}(x_1) & 1 & 0 & \ldots & 0 & 0 \\ I_1^{(p-1)}(x_2) & I_2^{(p-1)}(x_2) & \ldots & I_N^{(p-1)}(x_2) & 1 & 0 & \ldots & 0 & 0 \\ \cdots\cdots\cdots\cdots\cdots\cdots\cdots\cdots\cdots\cdots \\ I_1^{(p-1)}(x_N) & I_2^{(p-1)}(x_N) & \ldots & I_N^{(p-1)}(x_N) & 1 & 0 & \ldots & 0 & 0 \end{bmatrix},$$

$$\cdots\cdots\cdots$$

$$\widehat{\mathbf{I}^{(1)}} = \begin{bmatrix} I_1^{(1)}(x_1) & I_2^{(1)}(x_1) & \ldots & I_N^{(1)}(x_1) & \frac{x_1^{p-2}}{(p-2)!} & \frac{x_1^{p-3}}{(p-3)!} & \ldots & 1 & 0 \\ I_1^{(1)}(x_2) & I_2^{(1)}(x_2) & \ldots & I_N^{(1)}(x_2) & \frac{x_2^{p-2}}{(p-2)!} & \frac{x_2^{p-3}}{(p-3)!} & \ldots & 1 & 0 \\ \cdots\cdots\cdots\cdots\cdots\cdots\cdots\cdots\cdots\cdots \\ I_1^{(1)}(x_N) & I_2^{(1)}(x_N) & \ldots & I_N^{(1)}(x_N) & \frac{x_N^{p-2}}{(p-2)!} & \frac{x_N^{p-3}}{(p-3)!} & \ldots & 1 & 0 \end{bmatrix},$$

$$\widehat{\mathbf{I}^{(0)}} = \begin{bmatrix} I_1^{(0)}(x_1) & I_2^{(0)}(x_1) & \ldots & I_N^{(0)}(x_1) & \frac{x_1^{p-1}}{(p-1)!} & \frac{x_1^{p-2}}{(p-2)!} & \ldots & x_1 & 1 \\ I_1^{(0)}(x_2) & I_2^{(0)}(x_2) & \ldots & I_N^{(0)}(x_2) & \frac{x_2^{p-1}}{(p-1)!} & \frac{x_2^{p-2}}{(p-2)!} & \ldots & x_2 & 1 \\ \cdots\cdots\cdots\cdots\cdots\cdots\cdots\cdots\cdots\cdots \\ I_1^{(0)}(x_N) & I_2^{(0)}(x_N) & \ldots & I_N^{(0)}(x_N) & \frac{x_N^{p-1}}{(p-1)!} & \frac{x_N^{p-2}}{(p-2)!} & \ldots & x_N & 1 \end{bmatrix}.$$

Since $p = 6$ in the present study, Eqs. (A8)–(A11) become

$$\widehat{\frac{\partial^6 u}{\partial x^6}} = \widehat{\mathbf{I}^{(6)}} \widehat{w} = \mathbf{H}_6 \widehat{w}, \tag{A12}$$

$$\widehat{\frac{\partial^5 u}{\partial x^5}} = \widehat{\mathbf{I}^{(5)}} \widehat{w} = \mathbf{H}_5 \widehat{w}, \tag{A13}$$

$$\cdots$$

$$\widehat{\frac{\partial^2 u}{\partial x^2}} = \widehat{\mathbf{I}^{(2)}} \widehat{w} = \mathbf{H}_2 \widehat{w}, \tag{A14}$$

$$\widehat{\frac{\partial u}{\partial x}} = \widehat{\mathbf{I}^{(1)}} \widehat{w} = \mathbf{H}_1 \widehat{w}, \tag{A15}$$

$$\widehat{u} = \widehat{\mathbf{I}^{(0)}} \widehat{w} = \mathbf{H}_0 \widehat{w}. \tag{A16}$$

DATA AVAILABILITY

The data that support the findings of this study are available within the article.

REFERENCES

[1] S. V. Kostin, P. M. Krishenik, N. I. Ozerkovskaya, A. N. Firsov, and K. G. Shkadinskii, "Cellular filtration combustion of porous layers," Combust. Explos. Shock Waves **48**, 1–9 (2012).

[2] S. V. Kostin, P. M. Krishenik, and K. G. Shkadinskii, "Experimental study of the heterogeneous filtration combustion mode," Combust. Explos. Shock Waves **50**, 42–50 (2014).

[3] S. V. Kostin, P. M. Krishenik, and K. G. Shkadinskii, "Pulsating cellular regimes of infiltration combustion of porous media," Russ. J. Phys. Chem. B **9**, 385–391 (2015).

[4] D. Strunin, "Autosoliton model of the spinning fronts of reaction," IMA J. Appl. Math. **63**(2), 163–177 (1999).

[5] D. Strunin, "Phase equation with nonlinear excitation for nonlocally coupled oscillators," Phys. D Nonlinear Phenom. **238**(18), 1909–1916 (2009).

[6] A. Aldushin and T. Ivleva, "Hydrodynamic instability of the coflow filtration combustion: Numerical simulation," Dokl. Phys. Chem. **451**, 157–160 (2013).

[7] A. Aldushin and B. S. Braverman, "Saffman-Taylor problem in filtration combustion," Russ. J. Phys. Chem. B **4**, 788–792 (2010).

[8] S. Das and S. Puri, "Pattern formation in the inhomogeneous cooling state of granular fluids," Europhys. Lett. **61**, 749–755 (2003).

[9] I. Aranson and L. Tsimring, "Pattern and collective behavior in granular media: Theoretical concepts," Rev. Mod. Phys. **78**, 641–692 (2006).

[10] A. P. Aldushin, B. A. Malomed, and Y. B. Zel'dovich, "Phenomenological theory of spin combustion," Combust. Flame **42**, 1–6 (1981).

[11] M. C. Cross and P. C. Hohenberg, "Pattern formation outside of equilibrium," Rev. Mod. Phys. **65**, 851–1111 (1993).

[12] B. Kerner and V. Osipov, "Autosolitons," Phys.-Usp. **32**(2), 101–138 (1989).

[13] D. Strunin and M. Mohammed, "Range of validity and intermittent dynamics of the phase of oscillators with nonlinear self-excitation," Commun. Nonlinear Sci. Numer. Simul. **29**(1–3), 128–147 (2015).

[14] R. Bhanot and D. Strunin, "Dynamics of reaction fronts under a single-equation model," ANZIAM **57**(1–3), C398–C412 (2015).

[15] N. Mai-Duy and T. Tran-Cong, "Numerical solution of differential equations using multiquadric radial basis function networks," Neural Netw. **14**(2), 185–199 (2001).

[16] D. Ngo-Cong, F. Mohammed, D. Strunin, A. Skvortsov, N. Mai-Duy, and T. Tran-Cong, "Higher-order approximation of contaminant transport equation for turbulent channel flows based on centre manifolds and its numerical solution," J. Hydrol. **525**, 87–101 (2015).

[17] H. P. Langtangen and S. Linge, *Finite Difference Computing with PDEs—A Modern Software Approach* (Springer Nature, Cham, 2010).

[18] M. Mortensen, H. P. Langtangen, and G. N. Wells, "A FEniCS-based programming framework for modeling turbulent flow by the Reynolds-averaged Navier–Stokes equations," Adv. Water Resour. **34**(9), 1082–1101 (2011).

[19] R. Franke, "Scattered data interpolation: Tests of some methods," Math. Comput. **38**(157), 181–200 (1982).